

3D-Printed Regenerative Magnesium Phosphate Implant Ensures Stability and Restoration of Hip Dysplasia

Golafshan, Nasim; Willemsen, Koen; Kadumudi, Firoz Babu; Vorndran, Elke; Dolatshahi-Pirouz, Alireza; Weinans, Harrie; van der Wal, Bart C.H.; Malda, Jos; Castilho, Miguel

DOI

[10.1002/adhm.202101051](https://doi.org/10.1002/adhm.202101051)

Publication date

2021

Document Version

Final published version

Published in

Advanced Healthcare Materials

Citation (APA)

Golafshan, N., Willemsen, K., Kadumudi, F. B., Vorndran, E., Dolatshahi-Pirouz, A., Weinans, H., van der Wal, B. C. H., Malda, J., & Castilho, M. (2021). 3D-Printed Regenerative Magnesium Phosphate Implant Ensures Stability and Restoration of Hip Dysplasia. *Advanced Healthcare Materials*, 10(21), Article 2101051. <https://doi.org/10.1002/adhm.202101051>

Important note

To cite this publication, please use the final published version (if applicable).
Please check the document version above.

Copyright

Other than for strictly personal use, it is not permitted to download, forward or distribute the text or part of it, without the consent of the author(s) and/or copyright holder(s), unless the work is under an open content license such as Creative Commons.

Takedown policy

Please contact us and provide details if you believe this document breaches copyrights.
We will remove access to the work immediately and investigate your claim.

3D-Printed Regenerative Magnesium Phosphate Implant Ensures Stability and Restoration of Hip Dysplasia

Nasim Golafshan, Koen Willemsen, Firoz Babu Kadumudi, Elke Vorndran, Alireza Dolatshahi-Pirouz, Harrie Weinans, Bart C. H. van der Wal, Jos Malda, and Miguel Castillo*


Osteoarthritis of the hip is a painful and debilitating condition commonly occurring in humans and dogs. One of the main causes that leads to hip osteoarthritis is hip dysplasia. Although the current surgical methods to correct dysplasia work satisfactorily in many circumstances, these are associated with serious complications, tissue resorption, and degeneration. In this study, a one-step fabrication of a regenerative hip implant with a patient-specific design and load-bearing properties is reported. The regenerative hip implant is fabricated based on patient imaging files and by an extrusion assisted 3D printing process using a flexible, bone-inducing biomaterial. The novel implant can be fixed with metallic screws to host bone and can be loaded up to physiological loads without signs of critical permanent deformation or failure. Moreover, after exposing the hip implant to accelerated *in vitro* degradation, it is confirmed that it is still able to support physiological loads even after losing $\approx 40\%$ of its initial mass. In addition, the osteopromotive properties of the novel hip implant is demonstrated as shown by an increased expression of osteonectin and osteocalcin by cultured human mesenchymal stem cells after 21 days. Overall, the proposed hip implant provides an innovative regenerative and mechanically stable solution for hip dysplasia treatment.

1. Introduction

Osteoarthritis (OA) of the hip is a painful and debilitating condition that affects over 40 million people just in Europe.^[1,2] One of the main causes for hip OA is hip dysplasia (HD), which is an instability of the hip joint.^[3] This instability is caused by incomplete coverage of the femoral hip by the acetabulum^[4,5] and is commonly observed in humans, including children, as well as in veterinary patients, mainly dogs.^[6] The incorrect alignment of the hip joint in HD results in overload of the joint edges with subsequent degenerative changes of the cartilage and the acetabular labrum at a young age, leading ultimately to the development of osteoarthritis. Most HDs resolve without treatment or after bracing at early childhood.^[7] If HD remains during puberty, a very high risk of osteoarthritis results and often surgical treatment is required to correct the dysplasia by, e.g., realignment of the hip socket (osteotomy) or the insertion of a bone graft (shelf arthroplasty) to enlarge the

N. Golafshan, K. Willemsen, H. Weinans, B. C. H. van der Wal, J. Malda, M. Castillo
Department of Orthopaedics
University Medical Center Utrecht
Utrecht 3584 CX, The Netherlands
E-mail: M.DiasCastilho@umcutrecht.nl
N. Golafshan, J. Malda, M. Castillo
Regenerative Medicine Utrecht
Utrecht University
Utrecht 3584 CT, The Netherlands

F. B. Kadumudi, A. Dolatshahi-Pirouz
Department of Health Technology
Technical University of Denmark
Lyngby 2800, Denmark
E. Vorndran
Department for Functional Materials in Medicine and Dentistry
University of Würzburg
Würzburg 97070, Germany
H. Weinans
Department of Biomechanical Engineering
TU Delft
Delft 2628 CD, The Netherlands
J. Malda
Department of Clinical Sciences
Faculty of Veterinary Medicine
Utrecht University
Utrecht 3584 CL, The Netherlands
M. Castillo
Orthopaedic Biomechanics
Department of Biomedical Engineering
Eindhoven University of Technology
Eindhoven 5612 AZ, The Netherlands

 The ORCID identification number(s) for the author(s) of this article can be found under <https://doi.org/10.1002/adhm.202101051>

© 2021 The Authors. Advanced Healthcare Materials published by Wiley-VCH GmbH. This is an open access article under the terms of the Creative Commons Attribution-NonCommercial License, which permits use, distribution and reproduction in any medium, provided the original work is properly cited and is not used for commercial purposes.

DOI: 10.1002/adhm.202101051

acetabular rim.^[8] Osteotomies are technically demanding and invasive surgical procedures with associated complications, typically related to risk of nerve damage, inappropriate orientation of the acetabulum, and extensive rehabilitation periods.^[9,10] On the other hand, shelf arthroplasty is a less complex surgical procedure, but requires the use of bone grafts typically harvested from the patient's iliac crest, which can result in donor site morbidity.^[11] Moreover, the success rate of this procedure is relatively low, about 40% to 60%, due to the challenges in shaping and positioning of the bone graft to the defect size with associated accelerated graft resorption or impingement of the femoral head.^[12] There is thus, an urgent need for less invasive treatments that can overcome the drawbacks of the state-of-the-art procedures and subsequently ensure a near-perfect fit, facilitating optimal integration and durable restoration of the hip socket.

Progress in additive manufacturing (AM) techniques has provided new possibilities for the fabrication of individually shaped orthopedic implants. In particular, fabrication of titanium-based implants using a direct metal printing process has shown to generate personalized implants to treat hip dysplasia with a perfect repair of the bony defect and fit to the bone.^[13] Such a procedure can overcome the need for an osteotomy or shelf arthroplasty procedure. However, the use of metallic implants cannot ensure complete integration with native bone due to their nonresorbable properties and the implants may be associated with infection or loosening. In addition, the use of nonresorbable implants is not preferred for the treatment of younger (pediatric) patients due to mismatch of the implant size after patient growth.

Here, we developed a regenerative, yet stable, patient-specific bone implant for the treatment of hip dysplasia. The external and internal architecture of the implant was rationally designed to increase femoral coverage and mechanical stability. To manufacture the implant, a flexible and bone-inducing biomaterial ink, based on a magnesium phosphate (MgP) composite material,^[14] was extruded using an extrusion-based 3D printing process and sacrificial support material. After implant fabrication, the effect of the internal structure on mechanical stability and fixation to host bone was extensively investigated by three-point flexure and compression mechanical testing. To confirm the biocompatibility and osteopromotive properties of the biomaterial, printed constructs were in vitro cultured over 21 days using human mesenchymal stem cells. Finally, to anticipate the in vivo mechanical performance of the resorbable implant, implants were loaded under physiological loading conditions using a custom-built bioreactor system and after exposed to accelerated in vitro enzymatic degradation.

2. Results

2.1. Extrusion 3D Printing of Anatomically Shaped Hip Implants

Based on imaging data, the external implant design was adapted to provide adequate attachment to the pelvis and to provide the largest acetabular extension without impairing the range of motion of the femur (Figure 1A–C). Before being finalized for 3D printing, the anatomically designed hip implant was confirmed to not induce femoroacetabular impingement and to ensure a

perfect fit to the hip socket. Further, to allow for the fabrication of the implant's complex anatomical shape, we combined extrusion printing of a poloxamer hydrogel as a support material with extrusion of a MgPSr–poly(ϵ -caprolactone) (PCL) biomaterial ink in a single printing process using a printer set-up equipped with two printheads (Figure 1D). Both viscosity and density of the biomaterial ink were evaluated to ensure ink extrusion reproducibility. MgPSr–PCL showed a viscosity of ≈ 27.5 Pa s (Figure S1, Supporting Information) and a density of 1.7 g mL⁻¹.

Moreover, the implant's structure encompassed different architectures at the external and internal region of the implant (Figure 1E). The external region is made of a fully dense layer and the internal region is made of a porous region with an interfiber spacing of 1 and 0.7 mm (IFS-0.7 and IFS-1) (Figure 1F,G). These two interfiber spacings were investigated for optimal mechanical stability and have been selected based on best compromise between biomaterial ink printing accuracy and porosity (Figure S2, Supporting Information). We observed that independent of the internal architecture considered, the printed external architecture resembled well the CAD designed counterpart (Figure 1H, I). In addition, a final pore size of 606 ± 108 μ m and 319 ± 57 μ m was observed for IFS-1 and IFS-0.7 hip implants (Figure 1J), respectively. This resulted in a residual printing deviation from the CAD design for both internal architectures. Moreover, the final porosities of the IFS-1 and IFS-0.7 hip implants were observed to be $54.7 \pm 2.6\%$ and $46.1 \pm 1.2\%$, respectively (Figure 1K).

Subsequently, X-ray diffraction (XRD) analysis confirmed the presence of an MgPSr inorganic phase and PCL organic phase on the printed implants (Figure 1L). Notably, Scanning Electron Microscope (SEM) analysis on the implant microstructure showed that the ceramic phase was highly exposed and not masked by the PCL phase (Figure 1M; Figure S3A, Supporting Information). This was also confirmed by elemental analysis, which revealed the presence of Mg, P, and Sr ions at the surface of the 3D-printed hip implants (Figure 1N; Figure S3B, Supporting Information).

2.2. Effect of Internal Architecture on Implant Three-Point Flexural Properties

In order to evaluate the internal porosity on the mechanical performance of the generated implants, three-point bending tests were performed. Both IFS-1 and IFS-0.7 implant structures presented similar load–displacement behavior. Load–displacement curves started with a steep slope in the elastic region, followed by an inflexion point after the yield until maximum force was reached. Afterward, the force decreased substantially and plateau after failure (Figure 2A). As expected, implant fractures were observed to occur in the regions that experienced high tensile stresses (Figure 2B, red arrow), and interestingly were observed to initiate at similar displacements for both implant porosities. The maximum flexural stress and flexural elastic modulus of the IFS-0.7 implant were ≈ 1.6 and 2.2 times higher than for the IFS-1 implant (Figure 2C,D), respectively. However, no significant differences were observed in flexure strain between both internal architectures (Figure 2E). In addition, the strain energy was 1.4 times higher for IFS-0.7 implants than for IFS-1 implants (Figure 2F).

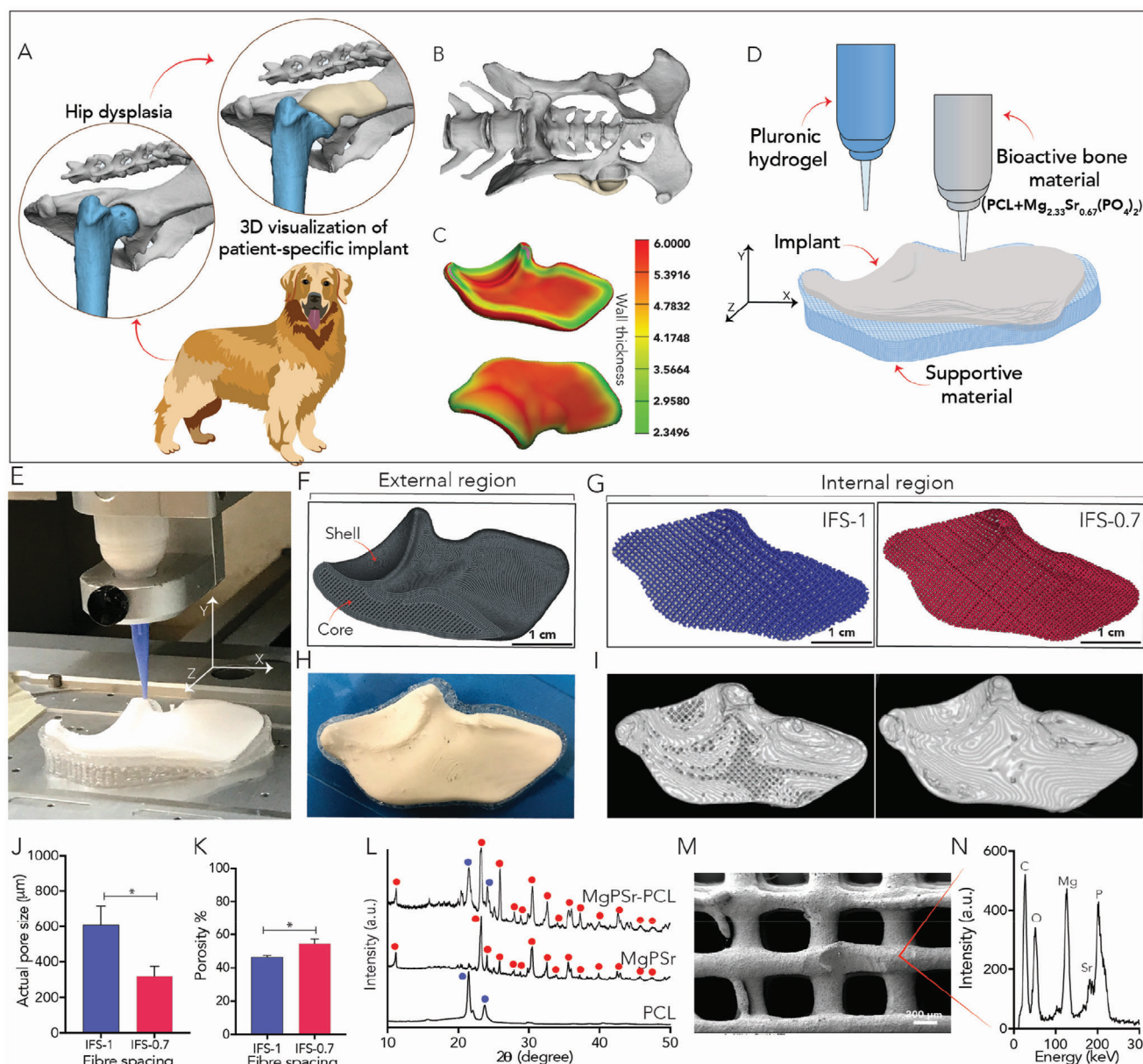


Figure 1. Design, fabrication, and respective printing accuracy and compositional analysis of the developed hip implants. A) Schematic illustration of the hip dysplasia in a canine model. B) CAD design of anatomically shaped implant based on patient image data. C) The wall thickness of the designed hip implants. D) Schematic illustration of extrusion 3D printing using a bone-inducing biomaterial ink and support material. E) Room-temperature extrusion-based printing process showing support material (transparent) and hip implant (white). F) Hip implant external and internal architecture, where G) internal architecture encompassed two interfiber spacings: 1 mm (IFS-1) and 0.7 mm (IFS-0.7). H) Representative image-printed hip implant shell region. I) 3D reconstructed micro-CT images of hip implants with IFS-1 and IFS-0.7 core region. J) Printed pore size for IFS-1 and IFS-0.7 and respective K) porosity (significant differences were analyzed by *t*-test, $n = 3$ and $*p < 0.05$). L) X-ray diffraction pattern of printed hip implants, with PCL identified with blue dots and MgPSr with red dots. Plain PCL and MgPSr were analyzed as controls. M) Representative SEM image of the hip implant with IFS-0.7 microstructure and respective N) EDX elemental analysis.

2.3. Flexible Biomaterial Ink Allows Stable Implant Fixation

The successful fixation of hip implants to the saw-bones using metallic screws was demonstrated (Figure 3A). The effect of implant porosity on fixation and stability upon cyclic shear loading was investigated by quantifying dissipated energy after cyclic shear loading at 100 and 200 N (Figure 3B) and respective implant

permanent deformation. Important to mention that a maximum shear load of 200 N was selected, as it would correspond to a force exerted on one of the hip quadrants of a dog with an average dog body weight of a 30 kg.

After the first loading cycle at 100 N, the energy dissipation is ≈ 1.2 times higher for the IFS-1 than IFS-0.7. Same trend was observed for samples loaded until 200 N, but with a significant

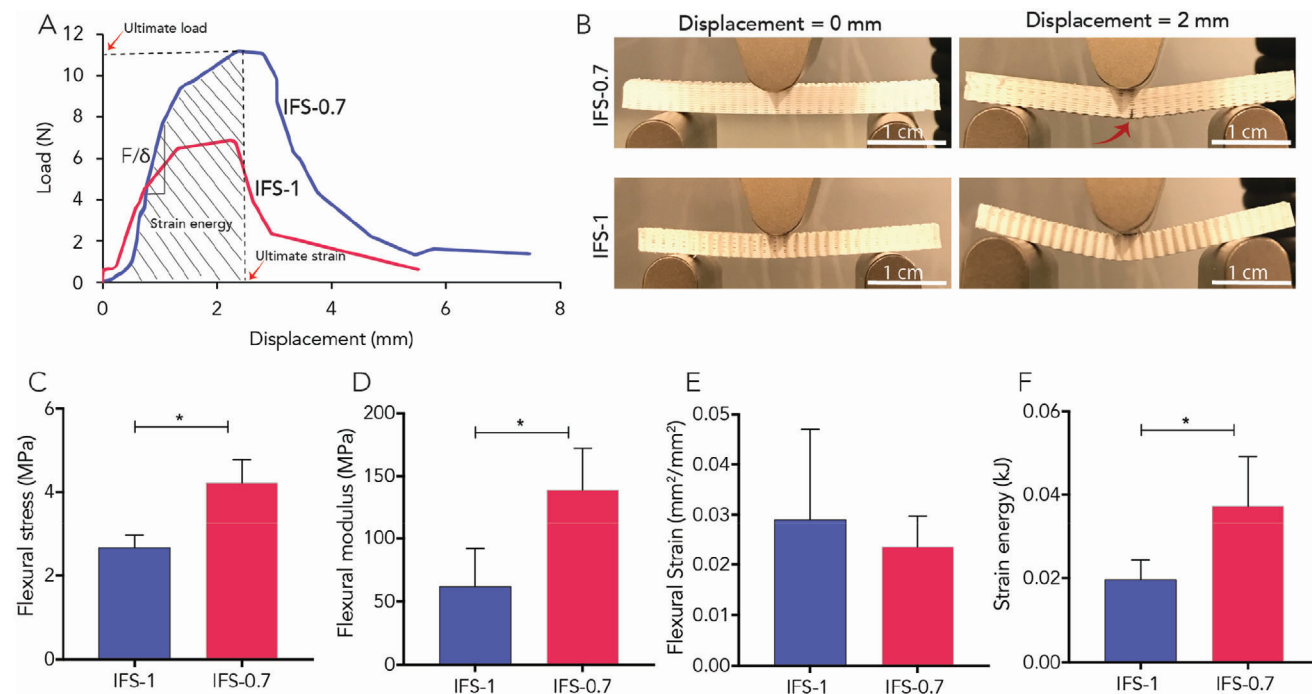


Figure 2. Flexure response under three-point loading of rectangular-shaped implant structures with different internal porosities. A) Representative load–displacement curves and B) corresponding photographs showing implants deformation before loading (displacement = 0 mm) and after loading (displacement = 2 mm). Determined C) flexural stress, D) flexural elastic modulus, E) flexural strain, and F) strain energy (significant differences were analyzed by one-way ANOVA, $n = 3$ and $*p < 0.05$).

higher dissipated energy, ≈ 2.3 times, for IFS-1 than for IFS-0.7 (Figure 3B). Furthermore, microcomputed tomography (micro-CT) analysis confirmed a higher permanent deformation of IFS-1 implants than of IFS-0.7 implants after cyclic loading (Figure 3C). The deformed shape of the fixation holes was approximated by an ellipsoid geometry and the deformation ratio quantified by $1+\epsilon_1$ (long axis) and $1+\epsilon_3$ (short axis) (Figure 3D,E). Permanent deformation was only statistically different between IFS-1 and IFS 0.7 implants at 200 N (Figure 3F). It should be noted that independently of the deformation observed, both internal architectures maintained their overall structural integrity through cyclic loading without failing even at higher applied forces than 200 N. Nevertheless, based on these fixation results and the results from three-point flexural characterization, we selected the IFS-0.7 implants for further evaluation since they presented negligible accumulated deformation and improved flexural properties.

2.4. Monitoring Implant Mechanical Integrity upon Degradation

We examined the microscopic features, as well as the mechanical performance of the implant internal structure upon accelerated in vitro enzymatic degradation. After 15 days of accelerated in vitro degradation, we observed that $38.5 \pm 1.1\%$ of the implant was degraded (Figure 4A). It is important to note that the lipase-enzyme medium solution used for the degradation tests catalyzes the implant degradation through hydrolysis, which is the major degradation mechanism in polymer-based scaffolds. Therefore, this allows us to resemble long term in vivo degradation in a relatively short in vitro experiment. In addition, the observed

degradation was accompanied by a sustained release of Sr^{2+} and Mg^{2+} (Figure 4B) without MgPSr major ceramic phase transformation, as confirmed by XRD analysis (Figure 4C). However, it is important to note, that the presence of $\text{Mg}(\text{H}_2\text{PO}_4)\cdot 2\text{H}_2\text{O}$ and $\text{Mg}(\text{H}_2\text{PO}_4)\cdot 4\text{H}_2\text{O}$ were also detected in the degraded implants which might be attributed to the hydration product of MgPSr. Furthermore, from the analysis of the flexural properties during in vitro degradation, we observed a significant decrease in maximal flexural stress and flexural modulus over the 15 days from 4.2 ± 0.6 MPa and 138.8 ± 33.2 MPa to 0.9 ± 0.5 MPa and 14.1 ± 4.7 MPa, respectively (Figure 4D–I). Interestingly, an increase in flexural strain was observed at day 10 and day 15. This might be attributed to the hydrolysis of the PCL bulk structure that resulted in high mobility of polymer chains and consequent increase in flexibility.

2.5. Cytocompatibility and Osteogenic Potential of Implants

In further analysis, we checked whether the biomaterial ink and 3D printing manufacturing strategy used resulted in toxicity of the produced implant or changes in their osteogenic potential. To investigate this, we benchmarked implants produced with biomaterial ink against PCL only implants. The human mesenchymal stem cells (hMSCs) proliferated faster on MgPSr–PCL implants than on PCL implants (Figure 5A). In addition, the metabolic activity analysis over 14 days also confirmed that the solvent-based printing approach did not affect cell activity and that cells, cultured on the MgPSr–PCL, were ≈ 1.4 times more active than when culture on pristine PCL implants after 14 days

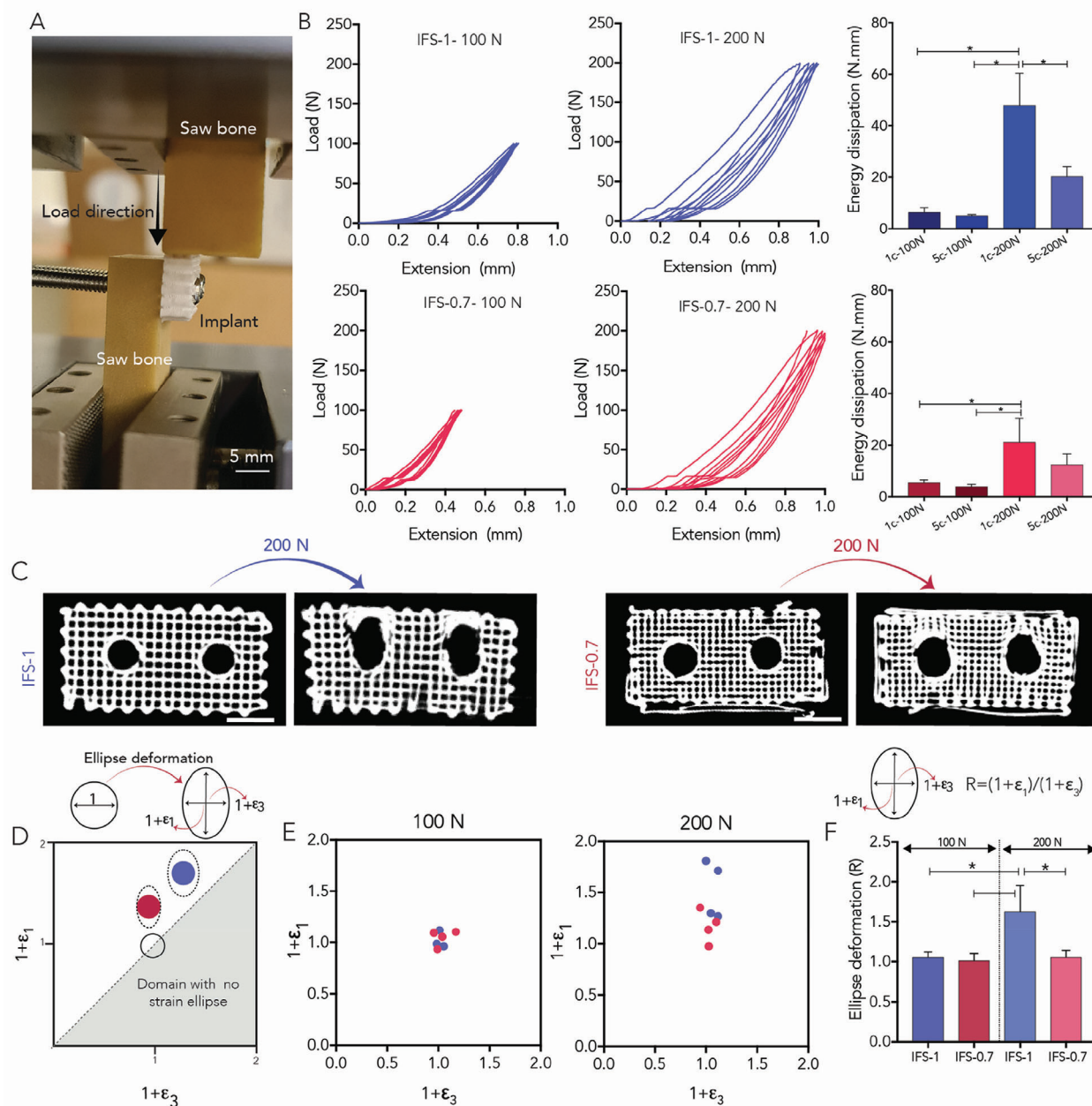


Figure 3. Fixation response of implants under cyclic shear loading. A) Snapshots image of the fixation of IFS-0.7 and IFS-1 to the saw-bones prior to the test. B) Representative load–extension curves at 100 and 200 N applied shear load and energy dissipation of the implants after one and five loading cycles. C) Representative micro-CT images of the unloaded (left) and loaded (right) implants at maximum shear load of 200 N (scale bar = 5 mm). D) Schematic of ellipse deformation parameters along the major (ϵ_1) and minor ellipse axis (ϵ_3) and E) respective experimental measured values. F) Ellipsoid deformation parameter R (significant differences were analyzed by one-way ANOVA, $n = 5$ and $*p < 0.05$).

(Figure 5B). Furthermore, the alkaline phosphatase (ALP) activity, as a measure of the osteogenic potential of the MgPSr–PCL implants, was three times higher than on PCL implants after 7 days of culture (Figure 5C,D). An upregulation of osteonectin (Figure 5E) and osteocalcin (Figure 5F), both markers of osteogenic differentiation, was also observed for cells cultured on the MgPSr–PCL scaffolds after 14 and 21 days of culture, confirming the osteoinductive potential of the hip implant biomaterial composition.

2.6. Ex Vivo Biomechanical Evaluation under Physiological Loading

To confirm the mechanical integrity of the hip implants under physiological loading, implants were tested in a custom-made biomechanical setup before and after accelerated in vitro degradation (Figure S5, Supporting Information). After 15 days in enzymatic media, implants did not exhibit a significant deterioration of their internal and external architecture, although the

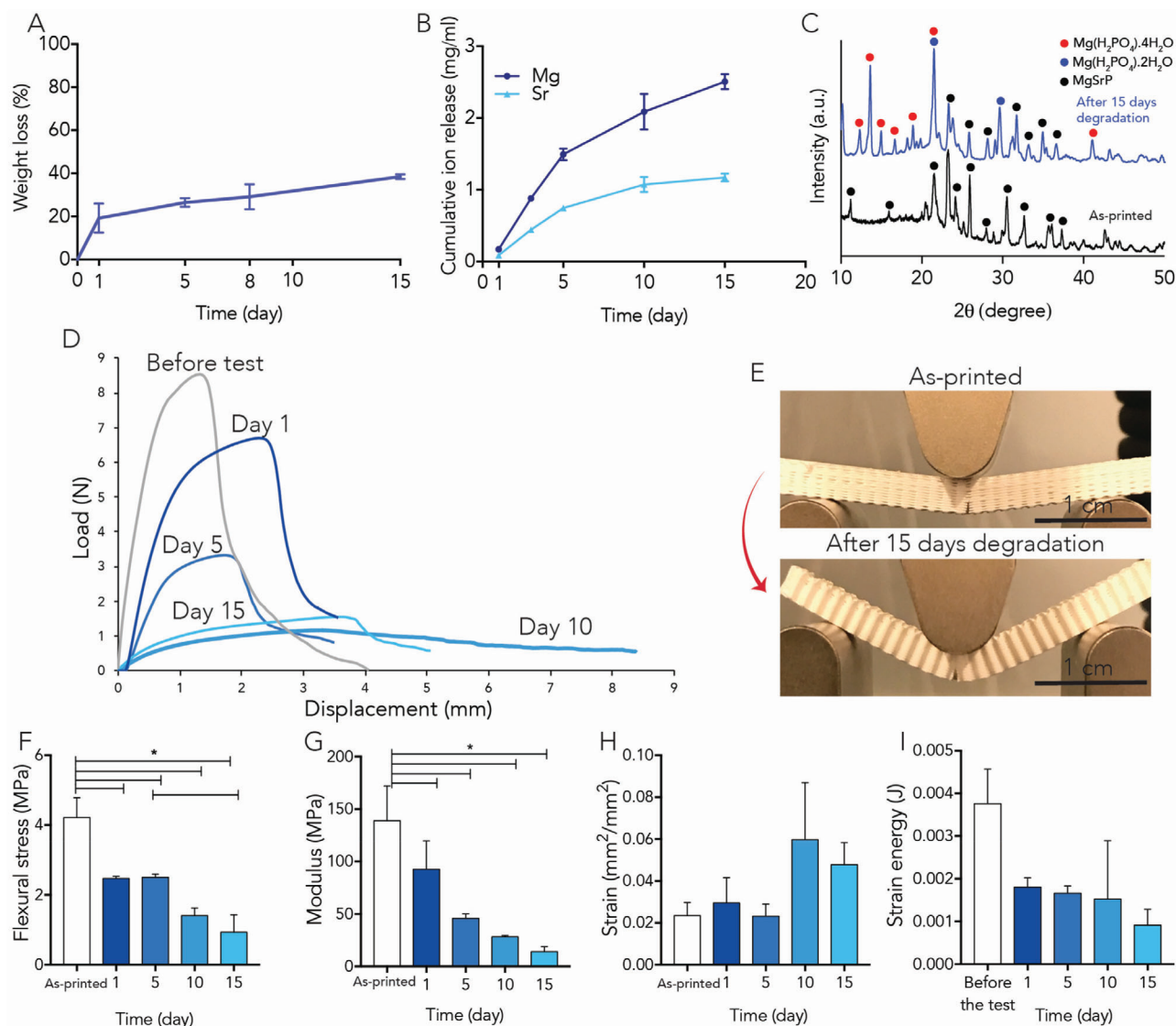


Figure 4. IFS-0.7 implant mechanical integrity and material composition stability upon in vitro enzymatic degradation. A) Implant weight loss, B) cumulative ion release, and C) XRD composition. D) Representative flexural load–displacement curves of IFS-0.7 implants at different time points of in vitro degradation and E) representative snapshots of as-printed and 15 days degraded implants after the flexural test failing. Determined F) flexural stress, G) flexural elastic modulus, H) flexural strain, and I) strain energy (significant differences were analyzed by one-way ANOVA, $n = 5$ and $*p < 0.05$).

presence of material voids and alternation of surface smoothness could be observed (Figure 6A). This material degradation resulted in a decrease in the overall mechanical performance of the implants when loaded under punctual compressive load (Figure 6A–E). In particular, after 15 days of degradation provided a material loss of 38.5% bringing the pore size from $(319 \pm 57) \mu\text{m}$ to $(524 \pm 21) \mu\text{m}$. At the same time the maximum load decreased from $(91.9 \pm 7.2) \text{ N}$ to $(18.7 \pm 2.9) \text{ N}$ ($p < 0.05$), while the overall implants stiffness dropped from $(36.8 \pm 6.9) \text{ N mm}^{-1}$ to $(13.4 \pm 1.2) \text{ N mm}^{-1}$. Moreover, a significant decrease in implants strain energy uptake from $(252.1 \pm 60.3) \text{ N mm}^{-1}$ to $(134.6 \pm 7.9) \text{ N mm}^{-1}$ was also observed. Local microscopic analysis of implants failure, revealed that failure was initiated close to the fixation screws (white arrows).

Although a significant decrease in mechanical properties was observed after 15 days of accelerated degradation, it was notable to observe that hip implant even after a loss in weight of material of $\approx 38\%$ did not lose completely its mechanical integrity.

3. Discussion

Currently, there is a great need for regenerative implants that could provide optimal integration and restoration of the hip socket as a regenerative and stable treatment for hip dysplasia. Here, we described the development of such implant by using extrusion 3D printing of a flexible, bone-inducing biomaterial ink and subsequently rigorously investigate its mechanical and (in vitro) biological performance.

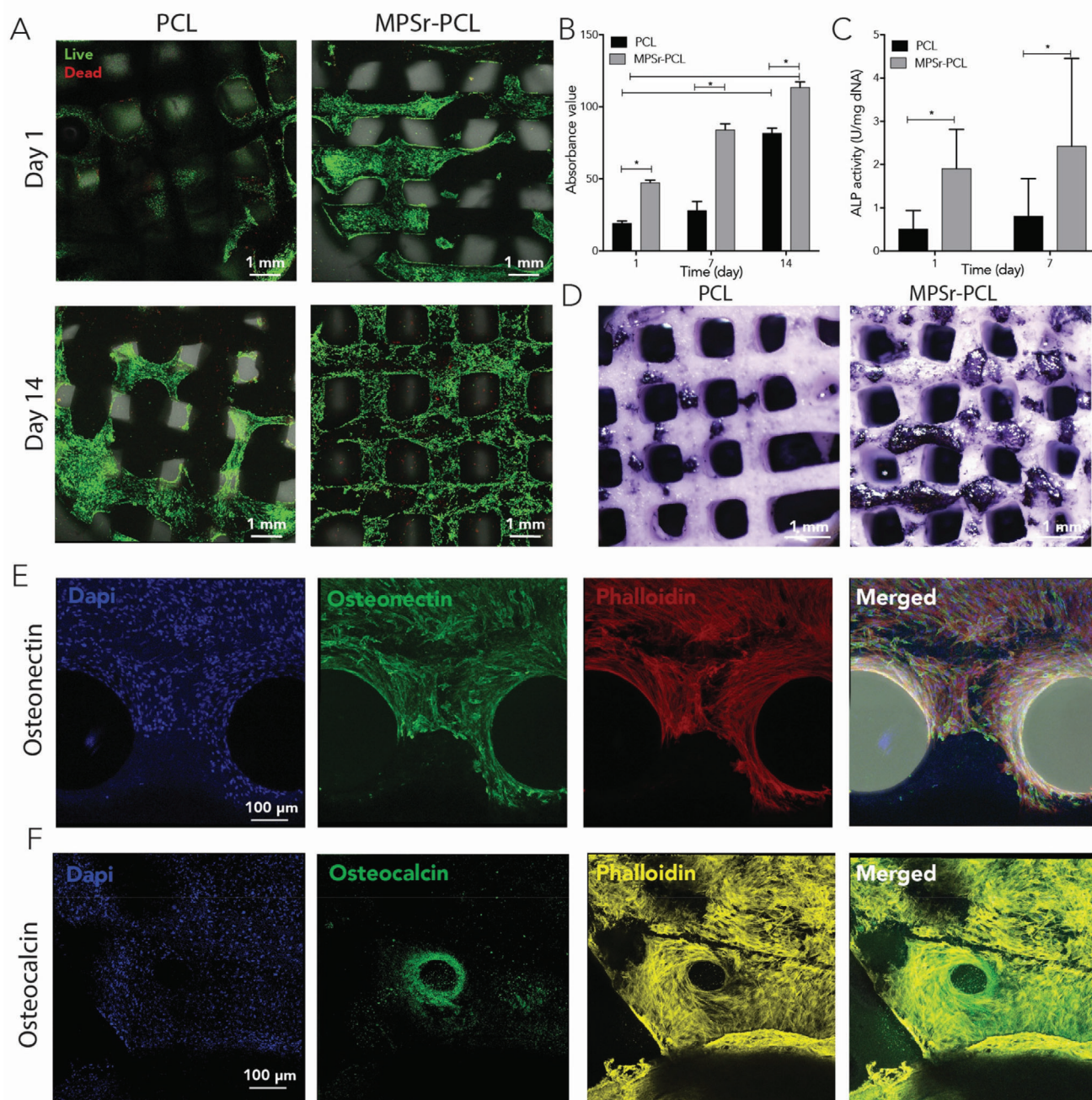


Figure 5. In vitro assessment of cytocompatibility and osteogenic potential of IFS-0.7 hip implants. A) Confocal images from the live–dead staining assay during 14 days culturing of hMSCs in basal media. B) Metabolic activity of hMSCs during 14 days culturing. C, D) Alkaline phosphatase (ALP) images of the printed samples. ALP activity levels were normalized to DNA content. E, F) Confocal images of osteonectin and osteocalcin expression in basal media after 14 and 21 days, respectively (significant differences were analyzed by two-way ANOVA, $n = 3$ and $*p < 0.05$).

The implant was designed based on CT scans of a dog hip joint. In an internal ongoing study, we have recently shown that a metallic hip implant with a similar design was able to provide an extension of the acetabular rim to keep the femoral head in its correct position, while still retained maximal range of motion of the hip joint. In the current work, local modifications on the implant thickness were specifically included to accommodate for

its resorbable properties, without compromising its mechanical stability. Moreover, we observed that the one-step extrusion-based printing strategy and the bone-inducing material combined here could yield a hip implant that uniquely matched the anatomical designed counterpart, with minimal geometrical deviation from CAD design. Important to mentioned that fabrication of such anatomically shaped and size relevant ceramic-based implants

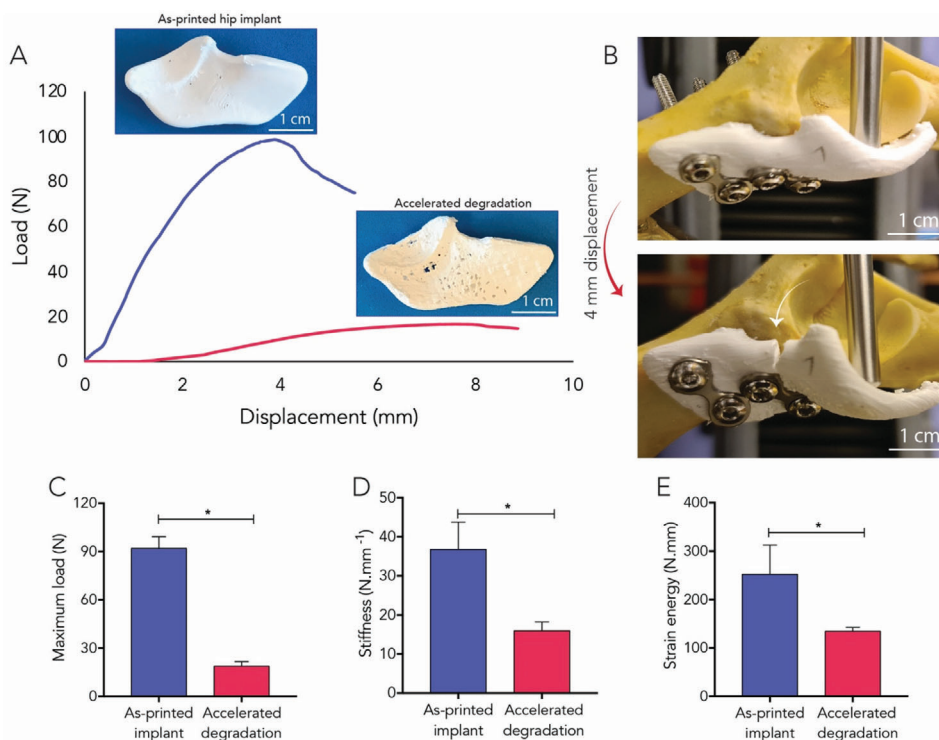


Figure 6. Mechanical performance of hip implants under physiological loading conditions for IFS-0.7. A) Load–displacement curves of as-printed implants and after 15 days immersing in enzymatic solution (accelerated degradation) and corresponding images of the hip implants. B) The snapshots of the as-printed and 15 days degraded implants after the failure. Determined C) maximum load, D) stiffness, and E) strain energy (significant differences were analyzed by one-way ANOVA, $n = 3$ and $*p < 0.05$).

is typically a limiting factor for the conventional extrusion-based printing processes when comparing to other technologies like 3D powder printing^[15,16] or stereolithography.^[17,18] The use of a sacrificial support material, together with the ceramic-based material ink that rapidly solidified due to presence of high volatile solvents, allowed to overcome this limitation.

In addition, through a rigorous mechanical evaluation, we confirmed that both the biomaterial ink and anatomically shaped implant with a highly porous and interconnected porosity can provide sufficient strength and resilience to support physiological loads. In particular, we first tested the effect of hip implants internal structure under three-point flexure. This allowed us to characterize both material and internal structure behavior, under simultaneous compression and tension loading, which the hip implants are known to be subjected to *in vivo*.^[19] As expected, we observed that internal porosity plays a significant role in the final implants mechanical performance, and that the low porosity implants (IFS-0.7) resulted in higher strength and flexural modulus. The flexural strength was largely dictated by the size of pores, therefore, the mechanical properties of IFS-1 was inferior to the IFS-0.7. Moreover, the obtained flexural strength of the hip implant internal architecture was approximately one order of magnitude higher than other previously reported ceramic-based bone implants.^[20] For example, calcium phosphate-based scaffolds obtained by casting of the cement paste were reported to present flexural strengths ranging from 3.1 to 4 MPa for a macroporosity between 40% and 50%. Low flexural and tensile strength has so far restricted the application of ceramic-based materials to non-

load bearing areas. Thus, our novel magnesium-based biomaterial demonstrates the potential not only to be shaped in complex geometry implants, but importantly to be used in load-bearing applications.

It is also important to notice that the flexible nature of the biomaterial ink allowed a stable fixation with metallic screws, which is not possible for most of the pure ceramic-based implants due to their brittle nature.^[20,21] Although a significant permanent deformation was observed upon loading on the IFS-1, which was mostly attributed to its highly porous internal architecture, the IFS-0.7 only showed only a residual permanent deformation at the implant fixation interface upon cyclic loading at 200 N (approximate maximum load exerted on one of the hip quadrants of a dog with an average bodyweight of 30 kg^[22,23]). Therefore, only hip implants with the internal porosity of IFS-0.7 were selected for *in vitro* biological evaluation and bioreactor study.

Through cytocompatibility and osteogenic differentiation studies, without the addition of osteogenic factors, we confirmed that the biomaterial ink (and printing strategy adopted) is not cytotoxic and can stimulate osteogenic differentiation of clinically relevant hMSCs. The cytocompatibility of the implants was attributed to the high volatility of the solvent combination used, which did not leave any toxic residues within the printed implant independent of its large volume and geometrical complex shape. This is particular important for future clinical translation of the hip implants. Furthermore, we were able to confirm the osteopromotive potential of the hip implants. The osteogenic differentiation of hMSCs was attributed to the high exposure of the MgPSr

ceramic phase on the implant structure and to the consequent release of Mg^{2+} and Sr^{2+} ions, which are both known to significantly promote bone formation.^[24,25] Importantly, the degradable characteristics and osteopromotive properties of the biomaterial ink combined with its high porous internal architecture, is expected to maximize bone ingrowth and consequent hip implant stability and fast integration with host bone. This will finally offer a viable alternative to the existent metallic hip implants, with particular impact for pediatric patients.^[26,27]

Moreover, despite the regenerative and osteopromotive properties of the hip implant, it is also fundamental that the mechanical integrity of the implants is preserved during the degradation process and properly balanced with bone ingrowth speed.^[14] We opted to study the in vitro acceleration degradation in the presence of lipase since it is known to hydrolyze PCL, which comes closer to the in vivo condition (as the degradation starts from the surface) than other conventionally used enzymes, such as Cutinase.^[28] Interestingly, the implants weigh loss here observed is in line with our previous findings in an in vivo study using an equine tuber coxae model.^[14] Importantly, the decrease in mechanical properties followed by in vitro degradation is in line with other reports on ceramic-based implants.^[29]

Our results also demonstrated that the developed hip implant can support a load exerted on the acetabulum of a dog with an approximate body weight of 30 kg, even after a material degradation of ≈ 38 wt% was observed. Important to mention, that the implant stability is expected to further improve after implantation due to resorbable nature and porous structure of the implant which will result in bone ingrowth into the porous structure, which typically occurs within 4–12 weeks post implantation.^[30] Therefore, it is likely that any initiation of failure observed in our study, as a result of degradation of the implant, will be compensated by the additional stability provided by bone ingrowth.

4. Conclusion

In conclusion, we have designed, fabricated, and fully characterized a patient-specific hip implant for hip dysplasia treatment. The patient-specific design was precisely fabricated from a flexible bone-inducing biomaterial using printed (sacrificial) supporting structures. Moreover, the implant was strong and resilient enough to bear physiological loads, is cytocompatible, can stimulate in vitro bone growth, and has the ability to resorb in vivo. This new regenerative implant opens a new perspective for the treatment of hip dysplasia of both veterinary (and potentially) human patients.

5. Experimental Section

Preparation of the MgP Biomaterial Ink: Printable biomaterial ink was prepared by combining $Mg_{2.33}Sr_{0.67}(PO_4)_2$ powder and commercial medical grade poly(ϵ -caprolactone) (mPCL, Purasorb PC 12, Purac Biomaterials, The Netherlands) in weight ratios of 70:30 wt% of MgPSr to PCL, according to a procedure previously described.^[14] Briefly, the ceramic component was synthesized by sintering (1050 °C, 5 h) a mixture of 0.6 mol magnesium hydrogen phosphate ($MgHPO_4 \cdot 3H_2O$, Sigma-Aldrich, Steinheim, Germany), 0.1 mol magnesium hydroxide ($Mg(OH)_2$, VWR International GmbH, Darmstadt, Germany), and 0.2 mol strontium carbonate ($SrCO_3$, Sigma-Aldrich, Steinheim, Germany). The sintered cake was manually crushed with pestle and mortar followed by

wet grinding for 2 h in pure ethanol in a planetary ball mill (250 U min^{-1}) using 200 agate balls. Afterward, the cement powder was dried at room temperature. Then, the MgPSr powder and mPCL were dispersed in a mixture of high volatile solvents (dichloromethane (Sigma-Aldrich, Germany), 2-BU-1-(4-(diethylamino) anilino)-3-me-pyrido(1,2-*a*) benzimidazole-4-carbonitrile (Sigma-Aldrich, Germany), and dibutyl phthalate (Sigma-Aldrich, Germany)) in a ratio of 10:2:1 wt%, at the concentration of 90 wt% of solid material in solvent. After dispersion, the composite paste was left for homogenizing for ≈ 4 days on a roller mixer at room temperature before printing.

Biomaterial ink printability was first accessed according to a protocol described elsewhere.^[14] Briefly, a one-layer triangular-shaped structure with a fill-in pattern of straight lines at increasing interfilament spacings, from 0.5 to 1 mm, was printed. Then, the length of fused filament (fs), at each filament distance (fd), was quantified. Fs was normalized by the average of filament thickness (ft). Moreover, to evaluate effect of filament stacking on printing resolution, rectangular-shaped scaffolds (10 mm \times 20 mm \times 4 mm) with three different interfiber spacings were printed. As a measure of scaffolds printing accuracy, open pore ratio was quantified by

$$\text{Open pore ratio} = \frac{A_t - A_a}{A_t} \quad (1)$$

where A_t and A_a are a theoretical and actual pore areas, respectively. Open ratio varies between 0 (open) and 1 (close). All measurements were performed with Image J.

Design and Extrusion-Based 3D Printing of Implants: All dogs used for the current cadaveric research were terminated for other non-orthopedic related experiments by another research group from the same institution (UMCU) that worked under Ethical approval nr.2016.II.529.002. After termination, the cadavers were donated to our group to reduce the need for experimental animals. To design the hip implants, three cadaveric dogs (6 hips) were CT scanned (Siemens SOMATOM Definition AS, Siemens, Healthcare) with the following standardized parameters, 120 kV, 250 mAs, and 0.6 mm slice thickness. The segmentation was done semiautomatically using standardized bone threshold values (HU 226 - upper boundary) using an imaging processing software, Mimics Medical 21.0 (Medical v21.0, Materialise, Leuven, Belgium). The implant's rim was designed in 3-Matic software (Medical v12.0, Materialise, Leuven, Belgium) to add 30° of coverage to the dysplastic acetabular rim without interfering with the hip capsule or muscles (e.g., Rectus Femoris) when using the standard dorsolateral approach to the hip joint. Additionally, the external implant was designed to provide adequate scaffold material (average thickness, 4 mm) and surface area to fixate the implant to the pelvis with bone screws.

After assessment of the implant external geometry, BioCAM software was used to define the hip implant internal architecture and subsequently translate the design into a G-Code. The external region of the implant (shell) was kept closed, while for the internal region (core) of the implant, two interfiber spacings, 1 and 0.7 mm (abbreviated as IFS-1 and IFS-0.7, respectively), were considered (Figure S2, Supporting Information). Designed implants were fabricated by a multimaterial extrusion-based 3D-printing system (3D Discovery, regenHU, Switzerland) using the MgPSr-PCL biomaterial ink. The ink was transferred to a 10 mL syringe (Nordson EFD, USA) and extruded through a 22G conical nozzle, (diameter = 0.41 mm, Nordson EFD, USA) at pressure of 0.9 bar and collector speed of 6 $mm s^{-1}$. For the fabrication of the anatomically shaped hip implants, a supporting material, 40 wt% of poloxamer (Pluronic F-127, Sigma-Aldrich, Germany), was used. Poloxamer ink was dissolved for 24 h at 4 °C, transferred to 10 mL syringe, and extruded printed through a 27G conical nozzle (diameter = 0.2 mm) at room temperature. After the printing process using the poloxamer and biomaterial ink, the scaffolds were immersed in cold water for 3 h to remove the support material.

Physical and Chemical Characterization: Pore size and porosity were analyzed by micro-CT analysis. Micro-CT was performed using a Quantum FX-Perkin Elmer (μ CT, Quantum FX, PerkinElmer, USA). Hip implants were scanned at 90 kV tube voltage, 180 mA tube current, 30 μm resolution, and 3 min scan time. Volume fraction and respective porosity

of IFS-1 and IFS-0.7 was determined by measuring trabecular parameters in 3D μ CT images according to a protocol described previously.^[14] Briefly, the 3D scans of the implants were adjusted based on Bernsen thresholding method using ImageJ software. Next, the volume fraction (BV/TV) was measured with BoneJ plugin for a specific region of interest (ROI) and porosity (Φ) was determined as

$$\Phi = 1 - \frac{BV}{TV} \quad (2)$$

Moreover, the printing deviation of the prepared implants was quantified as

$$\text{Printing deviation} = \frac{V_p}{V_{CS}} \quad (3)$$

where V_p and V_{CS} represent volume of the printed implants (based on the micro-CT images) and CAD designed implants, respectively. The volumes were measured with Meshlab (v.2016). In addition, the phase composition of printed implants was analyzed by X-ray diffraction using monochromatic Cu-K α radiation was utilized. X-ray measurements were collected from $2\theta = 10^\circ$ – 40° with a step size of 0.02° . The inorganic phase composition of MgPSr was checked by reference patterns of the ICDD database (magnesium strontium phosphate, $Mg_2Sr(PO_4)_2$, PDF ref. 00-014-0206, $Mg(H_2PO_4) \cdot 2H_2O$, PDF ref. 00-39-0132, and $Mg(H_2PO_4) \cdot 4H_2O$, PDF ref. 01-075-1445).

3D-printed implant microstructure and elemental composition was analyzed by SEM (XL30SFEG, FEI, USA) and energy-dispersive X-ray (EDX; Bruker AXS, Germany), respectively. Prior to imaging, samples were coated with gold (thickness = 6 nm). Both SEM and EDX were performed at an acceleration voltage of 10 kV.

Rheological evaluation of MgPSr–PCL ink was performed on a rheometer (Discovery HR-2, TA instruments). Biomaterial ink was placed between parallel plates (20 mm in diameter) at a gap distance of 0.5 mm. Viscosity was recorded during an oscillatory shear rate sweep test (10 – 100 s^{-1}). Density of MgPSr–PCL ink was calculated based on the mass of a unit volume of the ink.

Three-Point Flexural Tests: Three-point flexural tests were performed in a universal mechanical testing device (Instron, Model 5967, UK) with a 1 kN load cell. For both designs (IFS-1 and IFS-0.7), rectangular bars ($6 \times 1 \times 0.5$ cm) were printed with printing parameters described in “Design and Extrusion-Based 3D Printing of Implants” section and loaded at a crosshead speed of 2 $mm\ min^{-1}$, with support and loading span at 40 and 20 mm, respectively, according to a protocol previously described.^[31] The flexural stress, strain, modulus, and strain energy were calculated according to the classic beam theory considering a linear elastic material behavior. In particular, flexural stress was estimated as

$$\sigma_f = \frac{3P_{max}L}{2bh^2} \quad (4)$$

where P_{max} is the maximum load on the beam, L is the length of the support span, and b and h are the width and thickness, respectively. Flexural strain (at P_{max}) was calculated as

$$\epsilon_f = \frac{6b\delta}{L^2} \quad (5)$$

where δ is the beam deflection under P_{max} at the midspan. The flexural elastic modulus was determined from the load–displacement curve as

$$E_f = \frac{FL^3}{4b\delta h^3} \quad (6)$$

where F/δ is the tangent of the initial straight-line (linear) portion of the load–displacement curve. Moreover, the strain energy (U) was determined by the area below the load–displacement curve until maximum peak load (P_{max}). At least five samples for each group were tested.

Implant Fixation: To study the effect of initial implant fixation to the host bone, rectangular-shaped implants ($2 \times 1 \times 0.4$ cm) for both IFS-1 and IFS-0.7 internal architectures were fixed to rectangular-shaped saw-bone blocks ($2 \times 1 \times 1$ cm) using cortical screws (diameter = 3.5 mm) and loaded in shear with a customized loading device. A crosshead speed of 2 $mm\ min^{-1}$ was applied until a maximum shear force of 100 and 200 N was reached. At each maximum shear force, loading was repeated for five consecutive cycles to investigate the capacity of the material to recover. The applied load and deformation were monitored and the dissipated energy (U_d) after unloading at first and fifth cycle was quantified as

$$U_d = \int_0^{\delta_u} F_t(\delta) d\delta - \int_{\delta_0}^{\delta_u} F_e(\delta) d\delta \quad (7)$$

where $F_t(\delta)$ and $F_e(\delta)$ are the loading function and the unloading function, respectively. δ_u is the total strain at the unloading point, and δ_0 is the permanent strain after unloading. To further investigate permanent deformation of the tested samples, the area of the screw fixation holes, before and after loading, was quantified by micro-CT analysis. Shape of the fixation holes before loading was approximated as a circle of unit radius, and after loading as an ellipsoid. The deformed shape of ellipse (R) was quantified as,

$$R = (1 + \epsilon_1) / (1 + \epsilon_3) \quad (8)$$

where ϵ_1 and ϵ_3 represent deformation along X and Y axes (minor and major axis of the ellipse). At least, five samples for each group were tested.

In Vitro Degradation Experiments: The effect of enzymatically induced degradation of the implant material was evaluated in vitro over 15 days, with intermediate time points 1, 5, 10, and 15 days, following a protocol described elsewhere.^[14] Rectangular-shaped samples ($4 \times 1 \times 0.5$ cm) were incubated in a 0.4 $mg\ mL^{-1}$ lipase solution (from *Pseudomonas cepacia*, Sigma-Aldrich, Germany) and 1 $mg\ mL^{-1}$ sodium azide (Sigma-Aldrich, Germany) at $37^\circ C$. Incubation medium was refreshed every 4 days. At each intermediate time point samples were washed generously with milli-Q water and kept in the desiccator until 48 h prior mechanical testing and weight assessment. Subsequently, the effect of in vitro degradation on material mechanical performance was evaluated by flexural properties under three-point flexural testing, following the protocol described previously in “Three-Point Flexural Tests” section. In addition, weight loss of the implants and pH of the incubation solution were monitored at each intermediate time. Finally, the cumulative ion release profile of magnesium and strontium ions was recorded utilizing inductively coupled plasma mass spectrometry (ICP-MS, Varian, Darmstadt, Germany) at each incubation time point.

In Vitro Cell Culture: To confirm the cytotoxicity and osteogenic potential of the bone-inducing implants, MgPSr–PCL and plain PCL cylindrical samples (diameter = 5 mm and height = 1 mm) with an internal architecture of IFS-0.7 were prepared and cultured in vitro with hMSCs (passage number 3) for 21 days. Samples were sterilized in 70 v/v% ethanol for 2 h followed by 30 min under ultraviolet (UV) light. hMSCs were first expanded for 7 days in α -MEM supplemented with 10% (v/v) fetal bovine serum (FBS), 0.2×10^{-3} M L-ascorbic-acid-2-phosphate (ASAP), and 1% (v/v) penicillin–streptomycin at $37^\circ C$ in a humidified atmosphere containing 5% CO_2 , and then seeded (passage number 4) onto implants at a density of $150\ 000$ cells cm^{-2} . After seeding hMSCs onto implants, constructs were cultured in basal media.

hMSCs viability was determined using a live–dead viability kit for mammalian cells (Invitrogen Life Technologies, USA), prepared according to the manufacturer’s instructions. Stained cell-laden constructs were imaged using a confocal microscope (Leica SP8X Laser Scanning, Germany) with 494 nm (green, Calcein) and 528 nm (red, EthD-1) excitation filters. In addition, cell metabolic activity was quantified by Alamar blue, following manufacturer’s instruction. Moreover, hMSCs osteogenic differentiation was measured using ALP analysis performed at day 1 and day 7 of in vitro culture, following a protocol described elsewhere.^[14] Briefly, ALP activity was measured using conversion of the *p*-nitrophenyl phosphate

liquid substrate system (pNPP, Sigma-Aldrich) and a serial dilution of calf intestinal ALP (Sigma-Aldrich, Germany) in TE-buffer. ALP results were normalized to DNA content from the same cell lysate used to measure ALP, using a Quan-iT-Picogreen-dsDNA kit (Molecular Probes, Invitrogen, Carlsbad, USA) following the manufacturer's instructions. In addition, ALP staining of hMSCs was assessed by utilizing a 5-bromo-4-chloro-3-indolyl phosphate/Nitro blue tetrazolium (BCIP/NBT, ThermoScientific, USA) solution. At least three samples were analyzed per group, i.e., MgPSr-PCL and plain PCL cylindrical samples.

The implants and attached hMSCs were fixed 30 min in formalin to prepare for osteonectin and osteocalcin immunocytochemistry. Then, the cell-laden implants constructs were incubated for 10 min in 0.2% (v/v) Triton X-100 in PBS, and thereafter blocked for 30 min with 5% (v/v) bovine serum albumin/PBS. The samples were incubated overnight at 4 °C with 10 mg mL⁻¹ rabbit monoclonal anti-SPARC antibody (osteonectin, ab225716) and mouse monoclonal antibody recognizing human osteocalcin (clone OCG4; Enzo Life Sciences), respectively. This was followed by incubation with 10 mg mL⁻¹ goat-antimouse polyclonal antibody conjugated to Alexa Fluor 488 (Invitrogen). All cell-laden implants were also stained for F-actin (TRITC) and DAPI (FAK100 Kit; Merck Millipore), according to the manufacturer's protocol. All other fluorescence images were taken with a Leica SP8X Laser Scanning Confocal Microscope using a white light laser (470–670 nm) and Leica LASX acquisition software.

Ex Vivo Biomechanoreactor Studies: To investigate the mechanical performance of hip implants under representative physiological loading conditions, hip implants (IFS-0.7 group) were mounted on an ex vivo macerated dog pelvis before and after accelerated in vitro degradation (15 days). The pelvis was embedded in epoxy resin (poly-pox THV 500, Poly-Service B.V. Amsterdam, The Netherlands) to facilitate implant loading. The implants were placed in their correct surgical position to repair the acetabular defect and mechanically loaded in Y-direction to mimic normal gait of the canine.

A universal mechanical testing device (Instron, Model 5967, UK) equipped with a 1 kN load cell was used. Implants were loaded at a compressive speed of 5 mm min⁻¹ until implant (or pelvis) failure was reached. From the load–displacement curves different mechanical parameters were determined, in particular the load at failure (defined as the maximum load before implant failure), the strain energy (determined as detailed in “Implant Fixation” section), and the stiffness (as the slope of the load–displacement curves between 2 and 3 mm deformation). A minimum batch of three samples before and after 15 days of in vitro degradation was tested.

Statistical Analysis: A one- or two-way ANOVA with post-hoc Tukey's test was performed to compare the means of the different groups. Only for the pore size and porosity, normality and homogeneity were first checked with Kolmogorov–Smirnov test and then means of the groups were compared with an independent *t*-test. Differences were considered significant at a probability error (*p*) of *p* < 0.05. Data were represented as mean ± standard deviation (SD) and at least three samples were evaluated for each test. All statistical analysis was performed using GraphPad prism V6.

Supporting Information

Supporting Information is available from the Wiley Online Library or from the author.

Acknowledgements

The authors gratefully thank the following agencies for their financial support: the strategic alliance University Medical Center Utrecht-Technical University Eindhoven, the Gravitation Program “Materials Driven Regeneration”, funded by the Netherlands Organization for Scientific Research (024.003.013), and the partners of Regenerative Medicine Crossing Borders (RegmedXB) a public-private partnership that uses regenerative medicine strategies to cure common chronic diseases. This collaboration project is financed by the Dutch Ministry of Economic Affairs by means of the PPP Allowance made available by the Top Sector Life Sciences & Health

to stimulate public-private partnerships. The authors thank Morteza Alehosseini for all support and discussions with the biomaterial ink material characterization. After initial online publication, reference [13] was added to the reference list on November 3, 2021. This does not affect the overall discussion and conclusions of the work.

Conflict of Interest

The authors declare no conflict of interest.

Data Availability Statement

Research data are not shared.

Keywords

3D printing, bone implants, bone regeneration, hip dysplasia, load bearing, patient-specific implants

Received: May 29, 2021

Revised: September 6, 2021

Published online: September 24, 2021

- [1] *The Burden of Musculoskeletal Conditions at the Start of the New Millennium: Report of a WHO Scientific Group*, World Health Organization, Geneva **2003**, p. 218.
- [2] S. R. Kingsbury, H. J. Gross, G. Isherwood, P. G. Conaghan, *Rheumatology* **2014**, *53*, 937.
- [3] S. Jacobsen, S. Sonne-Holm, *Rheumatology* **2005**, *44*, 211.
- [4] B. L. Gray, J. B. Stambough, G. R. Baca, P. L. Schoenecker, J. C. Clohisy, *Bone Jt. J.* **2015**, *97-B*, 1322.
- [5] S. Pun, *Curr. Rev. Musculoskeletal Med.* **2016**, *9*, 427.
- [6] C. Pascual-Garrido, F. Guilak, M. F. Rai, M. D. Harris, M. J. Lopez, R. J. Todhunter, J. C. Clohisy, *J. Orthop. Res.* **2018**, *36*, 1807.
- [7] R. Sakkars, V. Pollet, *J. Child. Orthop.* **2018**, *12*, 302.
- [8] R. Ganz, K. Klaue, T. S. Vinh, J. W. Mast, *Clin. Orthop. Relat. Res.* **1988**, *232*, 26.
- [9] J. C. Clohisy, A. L. Schutz, L. St. John, P. L. Schoenecker, R. W. Wright, *Clin. Orthop. Relat. Res.* **2009**, *467*, 2041.
- [10] I. Zaltz, G. Baca, Y. J. Kim, P. Schoenecker, R. Trousdale, R. Sierra, D. Sucato, E. Sink, P. Beaulé, M. B. Millis, D. Podeszwa, J. C. Clohisy, *J. Bone Jt. Surg., Am. Vol.* **2014**, *96*, 1967.
- [11] D. R. Maldonado, V. Ortiz-Declet, A. W. Chen, A. C. Lall, M. R. Mohr, J. R. Laseter, B. G. Domb, *Arthrosc. Tech.* **2018**, *7*, e779.
- [12] K. Willemsen, C. J. Doelman, A. S. Y. Sam, P. R. Seevinck, R. J. B. Sakkars, H. Weinans, B. C. H. van Der Wal, *Acta Orthop.* **2020**, *91*, 383.
- [13] K. Willemsen, M. Tryfonidou, R. Sakkars, R. M. Castelein, A. A. Zadpoor, P. Seevinck, H. Weinans, B. Meji, B. C. H. van der Wal, *J. Orthop. Res.* **2021**, 25133.
- [14] N. Golafshan, E. Vorndran, S. Zaharievski, H. Brommer, F. B. Kadumudi, A. Dolatshahi-Pirouz, U. Gbureck, R. van Weeren, M. Castilho, J. Malda, *Biomaterials* **2020**, *261*, 120302.
- [15] J. A. Inzana, D. Olvera, S. M. Fuller, J. P. Kelly, O. A. Graeve, E. M. Schwarz, S. L. Kates, H. A. Awad, *Biomaterials* **2014**, *35*, 4026.
- [16] M. Castilho, C. Moseke, A. Ewald, U. Gbureck, J. Groll, I. Pires, J. Teßmar, E. Vorndran, *Biofabrication* **2014**, *6*, 015006.
- [17] L. Elomaa, S. Teixeira, R. Hakala, H. Korhonen, D. W. Grijpma, J. V. Seppälä, *Acta Biomater.* **2011**, *7*, 3850.
- [18] K. Arcaute, B. Mann, R. Wicker, *Acta Biomater.* **2010**, *6*, 1047.
- [19] G. N. Duda, E. Schneider, E. Y. S. Chao, *J. Biomech.* **1997**, *30*, 933.

- [20] A. Paknahad, N. W. Kucko, S. C. G. Leeuwenburgh, L. J. Sluys, *J. Mech. Behav. Biomed. Mater.* **2020**, *103*, 103565.
- [21] S. de Lacerdas Schickert, J. A. Jansen, E. M. Bronkhorst, J. J. van den Beucken, S. C. Leeuwenburgh, *Acta Biomater.* **2020**, *110*, 280.
- [22] N. R. Ordway, K. J. Ash, M. A. Miller, K. A. Mann, K. Hayashi, *Vet. Comp. Orthop. Traumatol.* **2019**, *32*, 369.
- [23] S. N. Sangiorgio, D. B. Longjohn, J. L. Lee, J. D. Alexander, L. D. Dorr, E. Ebramzadeh, *J. Appl. Biomater. Biomech.* **2008**, *6*, 72.
- [24] L. Mao, L. Xia, J. Chang, J. Liu, L. Jiang, C. Wu, B. Fang, *Acta Biomater.* **2017**, *61*, 217.
- [25] S. Yoshizawa, A. Brown, A. Barchowsky, C. Sfeir, *Acta Biomater.* **2014**, *10*, 2834.
- [26] A. F. Mavrogenis, A. D. Kanellopoulos, G. N. Nomikos, P. J. Pappalopoulos, P. N. Soucacos, *Clin. Orthop. Relat. Res.* **2009**, *467*, 1591.
- [27] N. G. Grün, P. L. Holweg, N. Donohue, T. Klestil, A. M. Weinberg, *Innovative Surg. Sci.* **2020**, *3*, 119.
- [28] K. Shi, J. Jing, L. Song, T. Su, Z. Wang, *Enzymatic Hydrolysis of Polyester: Degradation of Poly(ϵ -Caprolactone) by *Candida Antarctica Lipase* and *Fusarium Solani Cutinase*, Elsevier B.V, Amsterdam **2020**.*
- [29] R. M. Felfel, I. Ahmed, A. J. Parsons, G. S. Walker, C. D. Rudd, *J. Mech. Behav. Biomed. Mater.* **2011**, *4*, 1462.
- [30] A. A. Hofmann, R. D. Bloebaum, K. N. Bachus, *Acta Orthop. Scand.* **2009**, *68*, 161.
- [31] ASTM C1161 -02 Standard Test Method for Flexural Strength of Advanced Ceramics at Ambient Temperature, <https://www.astm.org/DATABASE.CART/HISTORICAL/C1161-02.htm>, n.d.